https://doi.org/10.5194/egusphere-2026-970
Preprint. Discussion started: 5 March 2026

PALM-CO_2 (v01): A High-Resolution Urban CO_2 Transport Model with Anthropogenic and Biogenic Fluxes

Linfeng Li[1], Jie Zheng[1], and Fangxin Fang[1]

[1]Department of Earth Science and Engineering, Imperial College London, London, SW7 2AZ, UK

Correspondence: Linfeng Li (l.li20@imperial.ac.uk) and Jie Zheng (jie.zheng1@imperial.ac.uk)

Abstract.

We develop PALM-CO_2, a high-resolution urban carbon dioxide transport model with anthropogenic and biogenic carbon emissions. The model is based on an open-source urban flow large eddy simulation (LES) model, PALM, where we implemented a biogenic carbon emission module (Vegetation Photosynthesis and Respiration Model, VPRM) and customised output modules for carbon fluxes. PALM-CO_2 is validated through a case study in London, comprising an 8 by 8 km^2 domain covering the borough of Camden at a resolution of 10 m. Simulations are driven by reanalysis meteorological forcing and background CO_2 concentrations, while the hourly anthropogenic emissions at 10-m resolution are explicitly derived in this study. Validation against eddy-covariance flux measurements inside the study region confirms that the model captures the diurnal variation of the turbulent transport and anthropogenic emissions. Additional validation against monthly biogenic flux diurnal profiles at a deciduous forest site in Czech Republic further confirms the biogenic flux module. The simulations reveal strong spatial heterogeneity in near-surface CO_2 concentrations driven by building-induced turbulence, diurnal boundary layer evolution, and emission patterns. PALM-CO_2 provides a high-resolution framework for investigating CO_2 transport processes in complex urban and vegetated environments, providing improved quantification of urban emission sources.

1 Introduction

Greenhouse Gas (GHG) emissions cause global climate change, with carbon dioxide (CO_2) being the most significant contributor. To understand the impact of CO_2 emissions, physical models have been used for modelling carbon cycle and climate. The Coupled Model Intercomparison Project (CMIP) (Anav et al., 2013) compares 18 earth system models' ability to simulate global carbon cycle across land and ocean; the models provide important insights for stakeholders, for example, climate projections from these models are used in Intergovernmental Panel on Climate Change (IPCC) report.

In the global carbon budget (Friedlingstein et al., 2023) for 2013-2022, anthropogenic activities (fossil CO_2 and land-use change) account for 12.9 GtC per year, while land update is 3.3 GtC per year and ocean update is 2.8 GtC per year. The numbers show the imbalance of the emission caused by anthropogenic activities and the huge uptake provided by biospheres

https://doi.org/10.5194/egusphere-2026-970
Preprint. Discussion started: 5 March 2026

and natural processes. Accurately representing both anthropogenic emissions and biospheric CO_2 fluxes is therefore essential for reliable carbon dioxide modelling.

A large portion of emissions occurs in urban environment (Dhakal, 2010; Marcotullio et al., 2013) due to industrialisation and high population density – energy sector takes 40% - 80% of global energy-related carbon emissions. Urban environments exhibit strong spatial and temporal heterogeneity in emissions as a result of diverse land use, building morphology, and socioeconomic activities, leading to complex intra-urban emission patterns. For example, Christen et al. (2011) estimated carbon emissions for a Vancouver neighbourhood at a 50 m grid resolution using activity data from buildings, waste, and transportation, demonstrating how heterogeneous urban land use influences emission patterns. Smith et al. (2025) adopted land-use regression to model carbon dioxide mixing ratios in the San Francisco bay area, showing the great intra-urban variance of carbon emission patterns. These studies have indicated the complexity in spatial and temporal patterns of anthropogenic emissions.

For urban carbon transport modelling, anthropogenic emission inputs are typically derived from inventories at kilometre-scale or coarser resolution and must be spatially disaggregated to match the model grid. This downscaling process commonly employs surrogate variables such as population density, building data, traffic activity, and land-use. While the methodology for generating fine-scale emission map is acknowledged, it largely depends on the available data for the study area. Several urban inventories have achieved resolutions from 1 km down to 50 m by integrating activity data and remote sensing products (London Datastore, 2023; Christen et al., 2011; Järvi et al., 2019; Cai et al., 2023). However, representing both anthropogenic emissions and biogenic fluxes consistently at a high spatial-temporal resolution remains challenging, underscoring the need for integrated urban-scale modelling frameworks.

In addition to anthropogenic emission, biogenic fluxes can serve as a source or sink for atmospheric CO_2. Globally, biosphere is a net sink of CO_2. However, on the urban scale, the diurnal cycle of biosphere activities yields temporally varying biogenic fluxes. To represent these processes, biogenic carbon models have been developed that explicitly simulate the underlying biochemical mechanisms of vegetation photosynthesis and ecosystem respiration. For example, Gerbig and Koch (2024) applied the Vegetation Photosynthesis and Respiration Model (VPRM (Mahadevan et al., 2008)) to calculate biosphere-atmosphere exchange fluxes for CO_2 across Europe. At the urban scale, Järvi et al. (2019) introduced a new biogenic carbon model that accounts for both human metabolism and vegetation effects, while Stagakis et al. (2025) conducted an intercomparison of four different biogenic models, highlighting discrepancies between model formulations. These studies demonstrate that biogenic fluxes can substantially influence urban CO_2 budgets, yet their integration with high-resolution transport models remains limited.

To investigate the transport of atmospheric components, physically based urban flow models have been developed to resolve local meteorological conditions. These models are grounded in physical principles and solved numerically, enabling simulations at very fine spatial-temporal resolutions. The models have been widely used to study heatwave (Anders and Maronga, 2025) and pollution episodes (An et al., 2007), and local micro-climate's impacts on, for example, building energy usage (Pfafferott et al., 2020) and safety operations of air vehicles (Jiang et al., 2024) as well as urban ecosystems (e.g. vegetation degradation (Neves et al., 2018)). Such models generally take consideration of local urban topology including terrain height and building geometries, land types and vegetations, meteorological driving forces (e.g. wind and radiation), as well as anthro-

https://doi.org/10.5194/egusphere-2026-970
Preprint. Discussion started: 5 March 2026

pogenic activities (e.g. chemical emissions and heat fluxes). Examples of such models are PALM (Maronga et al., 2020) and DALES (Heus et al., 2010).

Beyond advancing the understanding of physical mechanisms, finer-resolution carbon transport models in urban environments are essential for accurately representing concentration fields, thereby improving the model's capability to infer urban emission sources from ground-based measurements. This has been widely acknowledged within air pollution studies, as fine-resolution modelling enhances exposure assessment and supports source attribution and mitigation strategies. In contrast, such approaches are less commonly applied in the CO_2 study. For example, Brunner et al. (2019) demonstrated that neglecting realistic vertical emission profiles can lead to substantial overestimation of near surface CO_2 concentrations by up to 14% in summer and 43% in winter – highlighting the importance of vertical resolution in modelling. The limited use of fine scale CO_2 transport modelling in urban environments may partly stem from the scarcity of dense observational datasets. This gap motivates the development of integrated, high-resolution modelling frameworks that consistently couple urban flow dynamics with both high spatial resolution anthropogenic CO_2 emission datasets and biogenic CO_2 fluxes.

In this study, we develop a high resolution urban CO_2 transport modelling framework (PALM-CO_2) with 10 m resolution in both the horizontal and vertical directions, coupled with a CO_2 emission inventory resolved at the same spatial scale. The model is built upon the PALM large eddy simulation (LES) system (Maronga et al., 2020), which provides an accurate representation of urban scale flows and turbulence. Within this framework, we implement a biogenic CO_2 flux module and incorporate anthropogenic emission inventories as external forcing, enabling the simultaneous simulation of transport processes and surface–atmosphere CO_2 exchange in complex urban environments.

To support urban-scale applications, we design a dedicated workflow to spatially disaggregate anthropogenic CO_2 emissions for the study area of London. This workflow generates a high resolution emission grid map at 10 m × 10 m resolution by integrating multiple sources of locally available urban geoinformation, including residential and commercial property datasets, gas consumption statistics, industrial point-source inventories, and detailed road network maps. These datasets are combined to apportion emissions consistently across urban surface types and activity sectors, ensuring compatibility with the PALM computational grid.

As a demonstration case, we apply the model to the London Borough of Camden, a densely built urban area characterized by heterogeneous land use and emission sources. The resulting simulations provide new insights into fine scale CO_2 transport mechanisms within the urban canopy layer and their interaction with spatially distributed anthropogenic and biogenic fluxes. By explicitly resolving urban morphology and emission heterogeneity, the proposed modelling framework offers a foundation for future urban carbon emission inversion studies and for improving the interpretation of ground-based CO_2 observations in cities. More broadly, the framework supports integrated analyses of urban carbon dynamics by linking fine-scale surface characteristics, sector-specific emission patterns, and atmospheric transport processes, thereby improving source attribution, uncertainty quantification, and the evaluation of mitigation strategies in complex urban environments.

https://doi.org/10.5194/egusphere-2026-970
Preprint. Discussion started: 5 March 2026

2 Model description: PALM-CO_2 (v01)

PALM-CO_2 (v01) is implemented within the PALM model system (Maronga et al., 2020), a large-eddy simulation (LES) framework designed for high-resolution simulations of atmospheric flow in complex urban environments. PALM explicitly resolves the dominant turbulent eddies while parameterizing subgrid-scale (SGS) motions, and provides a modular structure that supports detailed representations of urban morphology, land–atmosphere interactions, and scalar transport. Building upon these capabilities, PALM-CO_2 extends the existing trace-gas functionality of PALM to enable the simulation of urban-scale CO_2 transport coupled with spatially and temporally resolved surface fluxes.

2.1 PALM framework and LES formulation

In PALM, the transport of passive scalar quantities, including trace gases, is governed by the filtered scalar conservation equation (Maronga et al., 2020):

$$\frac{\partial \bar{s}}{\partial t} = -\frac{1}{\rho}\frac{\partial \rho \bar{u}_j \bar{s}}{\partial x_j} - \frac{1}{\rho}\frac{\partial}{\partial x_j}\left(\rho \overline{u_j'' s''}\right) + \chi_s, \tag{1}$$

where s is the concentration of the trace gas in kg/m^3, t is time, ρ is the density of dry air, u_j is the j-th component of velocity, x_j is the spatial coordinate, and χ_s is the source or sink term of the passive scalar. Variables with double prime ($''$) refer to the subgrid-scale (SGS) component of the corresponding variables, while the over-bar indicates the filtered quantities. The advection and SGS turbulent flux divergence terms are discretized using finite-difference schemes implemented in PALM, and SGS fluxes are parametrised via an eddy-diffusivity approach consistent with the LES formulation.

PALM-CO_2 leverages these existing scalar transport codes and augments them with dedicated modules to represent anthropogenic and biogenic CO_2 fluxes. These fluxes enter the scalar transport equation exclusively through the source or sink term χ_s , ensuring a clean separation between atmospheric transport processes and surface exchange parametrisations.

Figure 1 illustrates the overall structure of PALM-CO_2, including the coupling between the flow solver, the biogenic flux module, and the prescribed anthropogenic emission inputs.

2.2 Biogenic emission model

Biogenic CO_2 exchange is represented using the Vegetation Photosynthesis and Respiration Model (VPRM; Mahadevan et al., 2008), which parametrises the ecosystem-scale carbon uptake and release based on vegetation state and meteorological drivers. VPRM has been widely applied in regional and urban-scale carbon studies (Ahmadov et al., 2007, 2009; Pillai et al., 2010, 2011). The parameters in the VPRM model are typically fitted using measurements from local eddy-covariance flux towers. In this study, we select a set of parameters from WRF-Chem module (Skamarock et al., 2019) that has been calibrated using flux tower measurement in Europe (Lian et al., 2021).

In PALM-CO_2, VPRM computes gross primary production (GPP) and ecosystem respiration (RESP) using the following equations:

$$\mathrm{GPP} = \lambda \times T_{\mathrm{scale}} \times P_{\mathrm{scale}} \times W_{\mathrm{scale}} \times \mathrm{EVI} \times \frac{1}{1+\mathrm{PAR}/\mathrm{PAR}_0} \times \mathrm{PAR}, \tag{2}$$

https://doi.org/10.5194/egusphere-2026-970
Preprint. Discussion started: 5 March 2026

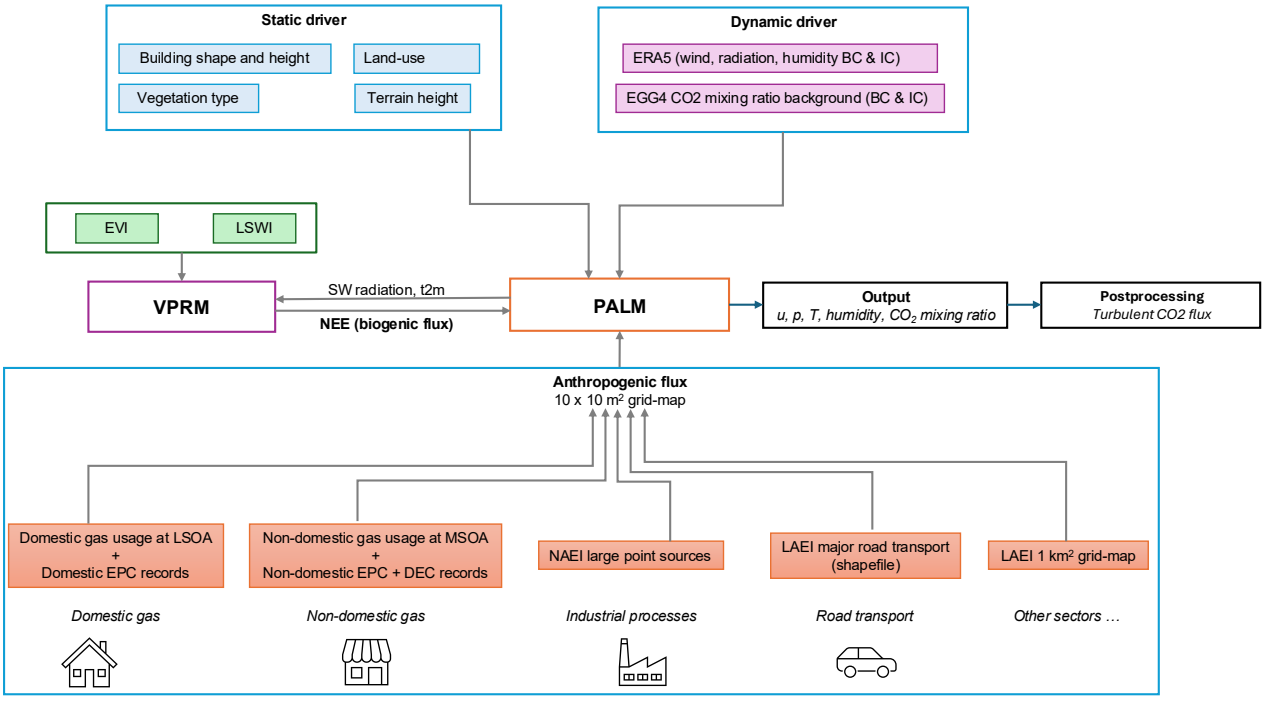

Figure 1. Flowchart of the model shows inputs, coupling between PALM and VPRM module, and the outputs.

where λ is a parameter fitted with the measurement of biogenic fluxes. Vegetation status and water stress are represented by the Enhanced Vegetation Index (EVI) and the Land Surface Water Index (LSWI). P_{scale} is a coefficient accounting for the degree of leafiness which is computed from LSWI and also depends on EVI to determine whether the vegetation has reached full leaf expansion. W_{scale} accounts for the water content in the vegetation and is computed from LSWI. PAR is photosynthetically active radiation which is correlated with short-wave (SW) radiation: $\text{PAR} \approx \text{SW}/0.505$; PAR_0 is a parameter for half photosynthetic saturation. T_{scale} is a coefficient computed from air temperature T,

$$T_{\text{scale}} = \frac{(T - T_{\text{min}})(T - T_{\text{max}})}{(T - T_{\text{min}})(T - T_{\text{max}}) - (T - T_{\text{opt}})^2}, \tag{3}$$

with T_{min}, T_{opt}, and T_{max} denoting minimum, optimal, and maximum temperatures for photosynthesis.

The respiration flux is mainly determined by the air temperature T and is computed from

$$\text{RESP} = \alpha T + \beta, \tag{4}$$

where α and β are coefficients that vary among different vegetation types; T_{air} is the air temperature. The net ecosystem exchange (biogenic flux) is then calculated

$$\text{NEE} = -\text{GPP} + \text{RESP}, \tag{5}$$

https://doi.org/10.5194/egusphere-2026-970
Preprint. Discussion started: 5 March 2026

where a negative value means net uptake and a positive value means net emission.

2.3 Diagnostic turbulent CO_2 fluxes

To facilitate comparison with eddy-covariance observations and to analyse vertical CO_2 exchange, PALM-CO_2 includes a diagnostic computation of turbulent scalar fluxes. The vertical turbulent flux (F) is defined as

$$F = \langle w's' \rangle, \tag{6}$$

where angle brackets denote the temporal average,

$$\langle \phi \rangle = \frac{1}{T} \int_{t_0}^{t_0+T} \phi(t) dt, \tag{7}$$

where T is the time window for averaging. w' and s' are the deviations from the mean of the vertical velocity component and tracer gas concentration (e.g. CO_2) respectively,

$$w' = w - \langle w \rangle, \tag{8a}$$

$$s' = s - \langle s \rangle. \tag{8b}$$

Then the flux can be computed from the following temporal averaged quantities,

$$\begin{aligned} \langle w's' \rangle &= \Big\langle (w - \langle w \rangle)(s - \langle s \rangle) \Big\rangle \\ &= \Big\langle ws - \langle w \rangle s - w\langle s \rangle + \langle w \rangle \langle s \rangle \Big\rangle \\ &= \langle ws \rangle - \langle w \rangle \langle s \rangle \\ &= \langle \bar{w}\bar{s} \rangle - \langle \bar{w} \rangle \langle \bar{s} \rangle. \end{aligned} \tag{9}$$

In the last line, the spatially filtered quantities $\bar{w}$ and $\bar{s}$ and their product $\bar{w}\bar{s}$ from the Large-eddy simulation (LES) code are used to compute the vertical turbulent flux for the CO_2 concentration. The temporal averaging of $\bar{w}\bar{s}$ is added to the code via a user-defined procedure. Its rolling sum is computed during time-stepping in the code, and its temporal average $\langle ws \rangle$ is computed and reported after each averaging time window T. $\langle w \rangle$ and $\langle s \rangle$ can be easily recorded using the default output settings in PALM. The time window for averaging is set as 0.5 hour.

2.4 Anthropogenic emission representation and disaggregation methodology

Anthropogenic CO_2 emissions for urban areas are commonly provided as coarse-resolution inventories, typically with a kilometre-scale spatial resolution, and as annual totals. For use in high-resolution urban transport models, such inventories must be disaggregated both spatially and temporally to match the computational grid and time step. A direct interpolation of

https://doi.org/10.5194/egusphere-2026-970
Preprint. Discussion started: 5 March 2026

coarse grid values onto a fine-resolution model grid is straightforward but insufficient to represent realistic urban emission patterns, which are often dominated by localised sources such as building heating systems, traffic corridors, and industrial point sources.

To address this, a sector-based disaggregation strategy is adopted. Emission sectors contributing only a small fraction of total emissions are distributed uniformly in space and time after interpolation to the fine grid. In contrast, dominant sectors are spatially disaggregated using additional geospatial surrogate data that represent the underlying emission-generating activities. This approach balances accuracy with data availability, as comprehensive surrogate datasets are not uniformly available for all emission sectors. The selection of sectors for detailed disaggregation is therefore based on their relative contribution to total emissions.

For sectors selected for fine-scale treatment, spatial disaggregation relies on auxiliary geospatial datasets such as building-level energy information, industrial point-source inventories, and road network data. These datasets are used as spatial proxies to redistribute emissions from coarse administrative or grid-based units to individual buildings, road segments, or point sources, which are then aggregated to the target model grid resolution.

Temporal disaggregation is applied to convert annual emissions into hourly fluxes. Sector-specific temporal profiles are used where available, capturing diurnal, weekly, and seasonal variability in anthropogenic activities. Sectors with negligible contributions are assigned constant temporal profiles, while dominant sectors employ time-varying profiles derived from established emission databases.

2.5 Implementation of PALM-CO_2 framework

PALM provides an interface for user-defined chemical mechanisms where one can set up the chemical components (Khan et al., 2021). In PALM-CO_2, CO_2 is represented as a single passive scalar without chemical reactions. Both anthropogenic and biogenic fluxes are treated as surface source terms and are incorporated into the scalar transport equation through χ_s in Eq. (1).

Biogenic CO_2 fluxes are computed by VPRM, whereas anthropogenic emissions are provided as externally prepared, time-resolved gridded datasets. VPRM is implemented in PALM as part of an online chemistry module, where biogenic fluxes are computed prior to solving the scalar transport equation using near-surface air temperature and short-wave radiation retrieved from PALM runtime variables. Anthropogenic emission sources (described in Section 3.2) are supplied as hourly NetCDF files, requiring activation of the level-of-detail (LOD) 2 option in PALM.

Both biogenic and anthropogenic fluxes are prescribed as source terms in the lowest atmospheric grid cell adjacent to the surface. In locations where complex terrain or building structures elevate the first fluid grid cell above ground level, the surface fluxes are applied at that elevated cell. This approach maintains a physically consistent coupling between surface emissions and the resolved airflow, ensuring that fluxes are introduced directly into the urban canopy layer where turbulent exchange and transport are explicitly represented.

https://doi.org/10.5194/egusphere-2026-970
Preprint. Discussion started: 5 March 2026

3 Case Study and Experimental Setup

3.1 Study area

A study area in London was selected for model validation and analysis, as shown in Figure 2. London is selected for its high population density, high level of urbanisation, and its vast amount of green infrastructures. In Camden, there is a CO_2 flux measurement station located at 190 m height on the BT tower (Helfter et al., 2011, 2016), providing an independent dataset for evaluating the performance of the model developed in this study.

The Greater London Authority (GLA) area (Fig. 2(a)) is characterised by a highly heterogeneous land-use and urban landscape. At its core lies a dense, multifunctional urban structure dominated by commercial, financial, and high-density residential uses, with extensive transport infrastructure and limited open space. Moving outward, land use transitions to predominantly residential neighbourhoods of medium to low density, interspersed with local centres, industrial estates, and major road and rail corridors. Despite its metropolitan character, the GLA area contains a substantial proportion of green and blue spaces, including large public parks, river corridors–most notably the River Thames–and protected areas (Wilby and Perry, 2006).

Sitting at the core of the GLA, the borough of Camden (Fig. 2(b)) reflects this heterogeneous landscape. From north to south, there is a mixing of green spaces (Hampstead Heath and the Regent's Park), residential area, and commercial and business centres around three main train stations (Euston, St Pancras and King's Cross). These are also shown in Figure 3 which depicts a bird's-eye view of dense building areas with parks and stations. Overall, land use in the GLA and Camden shows a complex mosaic in which intense urban development coexists with natural and semi-natural landscapes, resulting in strong spatial contrasts across relatively short distances.

A nested domain is used, which consists of a coarse-resolution domain (parent domain, denoted as N01 domain) and a fine-resolution domain (child domain, denoted as N02 domain). The parent domain (GLA)'s range is 60 km by 60 km in the horizontal and 3 km in the vertical, while the grid resolution in x, y, z is 100 m, 100 m, and 50 m respectively. The child domain (Camden)'s range is 8 km by 8 km in the horizontal and 1 km in the vertical, while the grid resolution is 10 m in all directions.

3.2 Anthropogenic emission datasets for London

For London case study, anthropogenic CO_2 emissions are derived from the London Atmospheric Emissions Inventory (LAEI) (London Datastore, 2023), published by the Greater London Authority. LAEI employs a bottom-up methodology, combining activity data with sector-specific emission factors to estimate emissions across multiple sectors. The most recent dataset available during this study is LAEI2019, released in 2022, which reports annual total emissions for the year 2019 on a 1 km^2 grid covering the region within the M25 motorway. The inventory grid conforms to borough boundaries, so that grid cells intersecting multiple boroughs are subdivided accordingly.

Since LAEI only reports annual total emission on 1 km^2 tiles, it is essential to further disaggregate the emission data spatially and temporarily for use in an urban model. A direct approach would be to interpolate the LAEI 1 km^2 tile data on the finite difference grid defined in the urban model. However, this approach cannot capture the real emission scenario where emission within a neighbourhood can originated from several large localised emission sources such as gas boilers within households or

https://doi.org/10.5194/egusphere-2026-970
Preprint. Discussion started: 5 March 2026

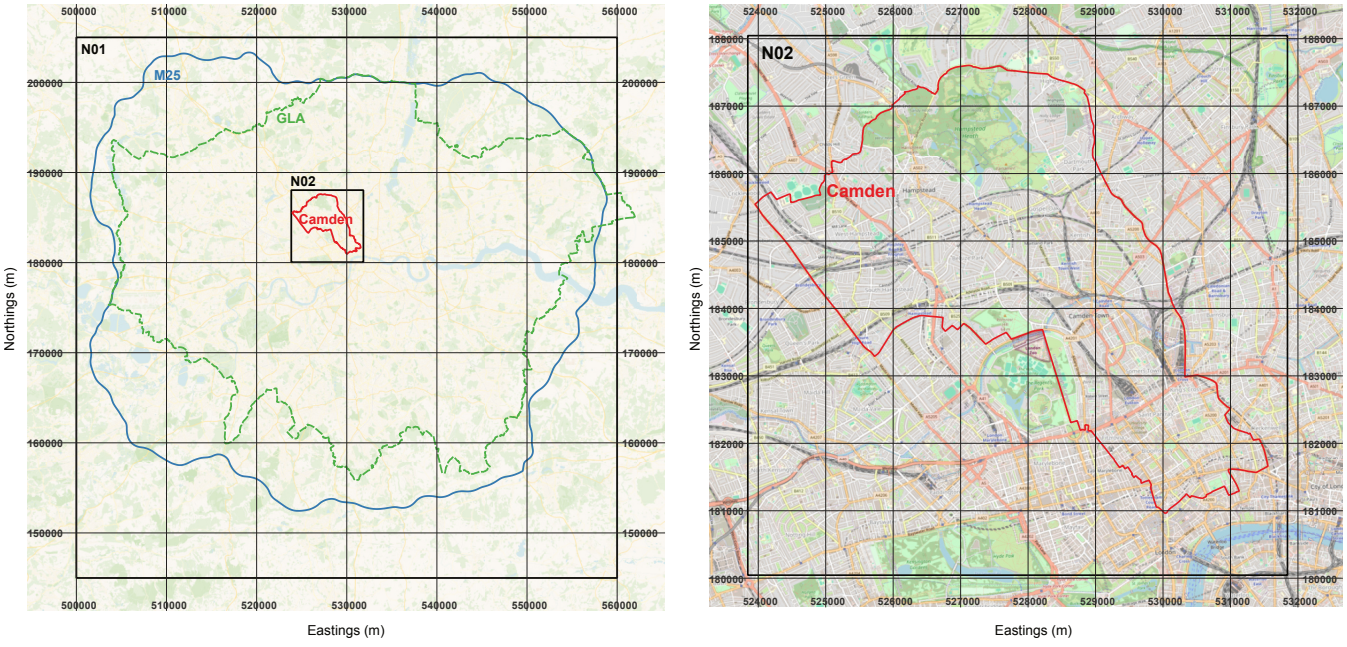

Figure 2. A nested study area surrounding M25 motorway and London Borough of Camden. The parent domain (denoted as N01) is roughly surrounding M25 motorway and the Greater London Area (GLA); the domain size is 60 km by 60 km. The child domain (denoted as N02) encompasses Camden and its size is 8 km by 8 km. Map data in the figure are from OpenStreetMap (OpenStreetMap contributors, 2017, ©OpenStreetMap Distributed under the Open Data Commons Open Database License (ODbL) v1.0 (for further information, please see https://www.openstreetmap.org/copyright/en)) and in British National Grid coordinate system.

industrial chimney stacks. While it is ideal to disaggregate all sectors into a fine grid map, there is a lack of available geo-spatial surrogate data for the task. For example, one might be able to find domestic building information in a city to disaggregate domestic energy usage sector, but there rarely exists a comprehend list of construction site for non-road mobile machinery sector. Therefore, one needs to decide which sectors should be disaggregated with additional surrogate data and which should be simply interpolated. Here, we examine the proportions of each sector in LAEI dataset. For sectors whose proportions are less than 10%, the sectors would be simply distributed evenly in the finer grid and in time (annual total amount spread to hourly emission). Otherwise, we consider them to be significant and require fine-scale geospatial data as spatial proxies to disaggregate. In LAEI, CO_2 emission is reported for four major sectors (domestic, commercial and industrial, transport, and others) with 17 sub-sectors. Figure 4 shows the significant emission sub-sectors, which are domestic gas combustion, non-domestic (commercial and industrial) gas combustion, road transport, and industrial processes A1 (A1 refers to large industrial point sources).

It is noted here that although the word “disaggregation” is used to describe the operation of processing emission inventory data to the desired grid resolution (10 m), data in LAEI for the following sectors are not used: the domestic gas combustion, the

https://doi.org/10.5194/egusphere-2026-970
Preprint. Discussion started: 5 March 2026

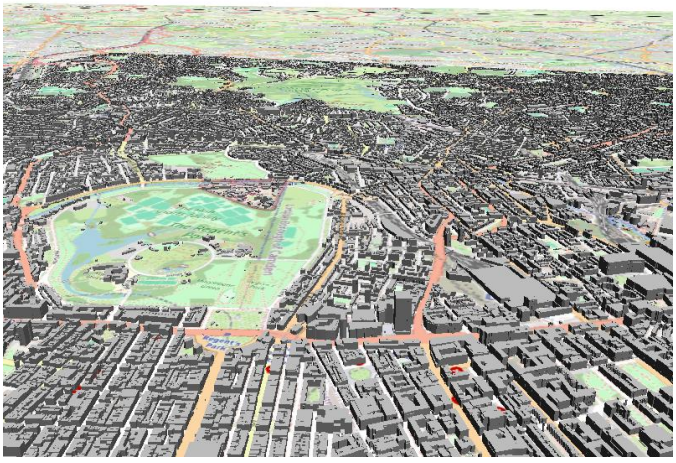

Figure 3. Bird's-eye view of buildings located in a region in the Camden borough. These building geometries are part of the static input for the PALM model. Data for the shape and height of buildings are from Ordnance Survey (Ordnance Survey (GB), 2019b, a). Background map is OpenStreetMap (OpenStreetMap contributors, 2017, ©OpenStreetMap Distributed under the Open Data Commons Open Database License (ODbL) v1.0 (for further information, please see https://www.openstreetmap.org/copyright/en)).

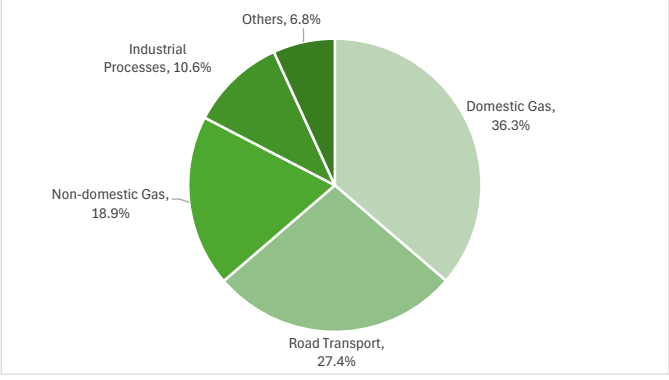

Figure 4. Major CO_2 emission sectors in the Greater London Authority region in 2019 – annual emission of sectors and their proportion in total emissions.

non-domestic gas combustion, and the industrial processes sectors. Instead, the source data for activities that LAEI has used to generate their 1 km^2 grid map are retrieved. Together with additional geospatial data as spatial proxies, we processed the 10 by 10 m^2 gird map for these sectors. Road transport was provided in LAEI as shapefile of the major road network and is convenient to interpolate to a grid of 10 by 10 m^2.

https://doi.org/10.5194/egusphere-2026-970
Preprint. Discussion started: 5 March 2026

3.2.1 Spatial disaggregation

Spatial disaggregation of four significant sectors uses additional geospatial data. These include gas usage within Lower-layer Super Output Areas (LSOAs) or Middle-layer Super Output Areas (MSOAs), industrial point sources inventory, and domestic and non-domestic properties' energy performance certificates (EPC).

For domestic gas combustion, activity data comes from official statistics published by Department for Energy Security and Net Zero in the UK (Department for Energy Security and Net Zero, 2015). The data repository records gas usage (in kWh) in lower-layer super output areas (LSOAs). Each LSOA is a statistical area covering 400 to 1,200 households and has 1,000 to 3,000 residents. To disaggregate gas usage in LSOAs to households, we obtain property records from Energy Performance of Buildings Data (Department for Levelling Up, Housing & Communities, 2025). Each record in the dataset includes an estimate of annual CO_2 emissions for the property which are used as a spatial proxy. This estimation is calculated from many characteristics of a domestic property, for example, the floor area, the floor height, its main heating fuel, and the status of wall and window. We filter domestic properties that use gas as the main fuel, and then utilise their annual CO_2 emissions as a spatial proxy to distribute the total gas usage in an LSOA to properties. Then, the sum of gas usage from domestic properties that falls within a title of 10 m by 10 m is taken as the gas usage for the tile. The spatial join operation between the domestic property dataset and the gas usage dataset was performed using the PostgreSQL database with the PostGIS extension. The gas usage in tiles is multiplied by emission coefficient 0.20566 $kgCO_2/kWh$ [1] to obtain annual emission in the grid map of 10 m by 10 m.

For non-domestic gas combustion, activity data also come from official statistics published by the Department for Energy Security and Net Zero in the UK (Department for Energy Security and Net Zero, 2015). Unlike domestic gas combustion, non-domestic gas usage statistics (measured in kWh) are reported at the Middle Layer Super Output Area (MSOA) level, which covers a larger geographical area than a Lower Layer Super Output Area (LSOA). Each MSOA contains around 5,000-15,000 residents or 2,000-6,000 households. To disaggregate gas usage in MSOAs to non-domestic properties, non-domestic energy records from Energy Performance of Buildings Data (Department for Levelling Up, Housing & Communities, 2025) are used, i.e. non-domestic EPC and DEC (display energy certificates). Unlike domestic records, many non-domestic records in this building dataset lack annual CO_2 emission estimation. Therefore, another `floor_area` attribute is used as a spatial proxy. Non-domestic properties that use gas as their main fuel are first filtered, and their floor areas are then used as a surrogate variable to apportion the total gas consumption within each MSOA to individual properties. The gas usage assigned to a 10 by 10 m^2 tile is calculated as the sum of the apportioned gas usage of all non-domestic properties intersecting that tile. The gas usage in tiles is multiplied by the emission coefficient 0.20455 $kgCO_2/kWh$ [2] to obtain annual emission in the 10 by 10 m^2 grid-map. It is noted here that the non-domestic heating and power sector has excluded industrial energy usage in LAEI. Therefore, non-domestic gas combustion only contains those in commercial and industrial properties, i.e. heating and power in such buildings.

[1] This emission coefficient for domestic gas consumption is from DESNZ report *Greenhouse gas reporting: conversion factors 2019* – Natural gas fuel, and has been tweaked to match to total annual emission of the sector in the LAEI region.

[2] This emission coefficient for non-domestic gas consumption is from Department for Energy Security and Net Zero report *Greenhouse gas reporting: conversion factors 2019* – Natural gas fuel.

https://doi.org/10.5194/egusphere-2026-970
Preprint. Discussion started: 5 March 2026

For road transport emissions, in addition to the 1 km^2 grid-map, LAEI presents a vector dataset of the London major road network stored in a shapefile. Each road sector in the shapefile has an attribute for annual transport emission. The shapefile can be rasterised into a 10 by 10 m^2 emission grid-map using spatial joint operation. The residual emissions from road transport (which is called minor road transport emission in LAEI) represent about 10% of the total road transport emission. These emissions are evenly distributed from the 1 km^2 grid to the 10 by 10 m^2 grid via interpolation.

The industrial processes in LAEI use data from both the Environment Agency's point source inventory[3] and the National Atmospheric Environmental Inventory[4]. These inventories include power plants, waster water processing factory, and other industrial sites. The point sources are spatially joined with the 10 by 10 m^2 tiles for a fine emission grid-map.

3.2.2 Temporal disaggregation

The temporal profiles of various sectors are used to disaggregate annual emissions into hourly emissions. Similarly as in spatial disaggregation, sectors with a proportion less than 1% are disaggregated using constant temporal profiles. The other sectors use temporal profiles retrieved from CAMS-TEMPO (Guevara et al., 2021) and EDGAR (Crippa et al., 2020). These sectors and their temporal profiles are listed in Table 1.

Table 1. Sectors and their temporal profiles. In "Reference" column, CAMS refers to CAMS-TEMPO (Guevara et al., 2021).

Sector	Temporal profile	Reference
Domestic - heat and power generation	Daily coefficients in years, hourly coefficients within a day	CAMS - Residential
Road Transport	Monthly, weekly, weekday / Saturday / Sunday+holiday daily profiles	CAMS - Transport
Industrial and commercial - heat and power generation	Monthly, weekly, daily profiles	CAMS - Energy
Industrial and commercial - industrial processes	Monthly, daily profiles	CAMS - Industrial
Transport - aviation	Monthly, weekly, daily profiles	CAMS - Aviation
Industrial and commercial - construction	Monthly, weekly, daily profiles	EDGAR - Construction

3.3 Vegetation indices and parameter selection

For the London case study, vegetation state variables required by the biogenic CO_2 flux model are derived from satellite-based surface reflectance products. Due to frequent cloud cover over the United Kingdom, EVI and LSWI are processed as monthly composites rather than at higher temporal resolution. For each calendar month in 2019, all available cloud-free satellite observations from the corresponding month throughout the 2018-2020 period are selected and temporally mosaicked.

[3]Accessible from https://www.data.gov.uk/dataset/cfd94301-a2f2-48a2-9915-e477ca6d8b7e/pollution-inventory
[4]Accessible from https://naei.energysecurity.gov.uk/data/maps/emissions-point-sources

https://doi.org/10.5194/egusphere-2026-970
Preprint. Discussion started: 5 March 2026

The median values are used to generate spatially complete monthly EVI and LSWI fields, reducing data gaps caused by cloud contamination.

The resulting monthly EVI and LSWI maps are provided to PALM as static input variables and are used by the biogenic flux module to represent vegetation phenology and water stress. This approach ensures spatial continuity of vegetation indices while preserving seasonal variability relevant for photosynthesis and respiration.

The parameters of the biogenic model are selected from the VPRM chemistry (WRF-Chem) weather research and forecast model (Skamarock et al., 2019), using parameter sets calibrated against measurements of the flux tower of eddy-covariance in Europe (Lian et al., 2021). These parameters are applied uniformly across the study domain, acknowledging that vegetation-specific calibration at the neighbourhood scale is not feasible given the available observations.

3.4 Diagnostic flux averaging configuration

To facilitate analysis of turbulent CO_2 exchange and comparison with eddy-covariance observations, temporal averaging of resolved vertical scalar fluxes is configured with a 30 min averaging window, consistent with standard flux tower processing conventions. The mean vertical velocity and CO_2 concentration are obtained from the standard PALM output, while the covariance term is accumulated online during model integration. The resulting averaged flux fields are output for post-processing and evaluation.

3.5 Modelling settings in PALM-CO_2

3.5.1 Static driver

As an urban model, PALM takes all the data describing urban land surface within one file called the static driver. These data include terrain height, land-use type and building geometries. The data sources for static inputs in the study area are listed in Table 2. The static input file is prepared with an open source tool GEO4PALM (Lin et al., 2024).

For buildings' geometry, the topography map from Ordnance Survey (OS) (Ordnance Survey (GB), 2019b) is used. The full topography map is filtered to include buildings only. For buildings' height, an additional OS building height dataset (Ordnance Survey (GB), 2019a) is used. The shapes (geometries) and the heights of buildings are matched with unique IDs indexed by OS to form a vectorised building map. For terrain height, two data sources of different resolution are selected for the parent and child domain, namely OS Terrain 50 (Ordnance Survey (GB), 2019c) (resolution at 50 m) and National Lidar Programme (Environment Agency, 2025) (resolution at 1 m). Land-use and vegetation types are retrieved from ESA WorldCover dataset (Zanaga et al., 2022).

Using these static input data, we activated the following urban surface modules. An urban surface module solves for the buildings' energy balance and energy exchange with outdoor environments. A land surface module computes the drag and heat dispersion in different land-use types, including vegetation, pavement, water, and soil. Land-use types also affect radiation from and into the urban surface. The soil temperature is modelled with an eight-layer energy balance equation.

https://doi.org/10.5194/egusphere-2026-970
Preprint. Discussion started: 5 March 2026

Table 2. Data sources for static and dynamic drivers in the study area.

Type	Data source
Terrain height	OS Terrain 50 (Ordnance Survey (GB), 2019c), National LiDAR @ 1 m (Environment Agency, 2025)
Buildings (shape and height)	Ordnance Survey topography map (Ordnance Survey (GB), 2019b), OS Building height attribute (Ordnance Survey (GB), 2019a)
Land-use and vegetation type	ESA WordCover @ 10 m (Zanaga et al., 2022)
EVI, LSWI	Sentinel-2 multispectral image @ 10 m (European Space Agency (ESA), 2025)
Meteorological condition	ERA5 @ 31 km, hourly (Hersbach et al., 2020)
CO_2 mixing ratio background	EGG4 @ 0.75°, 3-hourly (Copernicus Atmosphere Monitoring Service, 2021)

3.5.2 Initial and boundary conditions (dynamic driver)

The initial and boundary conditions are taken from real meteorological data from ECMWF reanalysis dataset (ERA5) (Hersbach et al., 2020). These are prepared as a "dynamic driver" file in PALM. ERA5 model level data for hourly velocity, potential temperature, humidity, long- and short-wave radiation, and surface level pressure are used to drive the urban model simulation.

For CO_2 transport, the background value of its mixing ratio is also required on the boundary outside the modelling region. This information comes from CAMS global greenhouse gas reanalysis (EGG4) (Copernicus Atmosphere Monitoring Service, 2021). 3-hourly CO_2 mixing ratio in the study region is used as the background value on the boundary. It is interpolated into hourly data and written in the dynamic file. These dynamic driven data sources are also listed in Table 2.

3.5.3 Running on HPC

The case is set up to running on ARCHER2 (UK HPC) using 1274 cores, out of which 250 cores are used for the parent domain (N01) with 10 by 25 subdomains in the x and y directions and the rest 1024 cores are used for the child domain (N02) with 32 by 32 subdomains in the x and y directions. The 16^{th} day of each month in 2019 is selected for the simulation at the study area. Depending on the average wind speed of the day, the CPU wall time for one day simulation takes between 6.1 h (for April 16th) and 23.2 h (for March 16th).

4 Results and discussion

4.1 Validation against BT tower measurement

In this subsection, we show comparison of the modelled flux and the measured flux by the eddy covariance method. This comparison validates: 1) the input emission sources and sinks from anthropogenic and biogenic activities, and 2) the CO_2 transport process calculated by PALM.

https://doi.org/10.5194/egusphere-2026-970
Preprint. Discussion started: 5 March 2026

In previous studies, CO_2 transport has been approximated using simplified two-dimensional advection–dispersion approaches, in which turbulent source areas or flux footprints were parameterized rather than explicitly resolved; see Christen et al. (2011) for an urban carbon emission model that leverages the 2D model for validation. In contrast, PALM resolves 3D turbulence using large-eddy simulation, enabling a more detailed representation of turbulent dispersion and vertical transportation processes, and thereby providing a more physically consistent characterization of source-receptor relationships.

The measurement site is in Camden, London. An eddy-covariance flux tower was set up on the BT tower in Camden by previous researchers (Wood et al., 2010; Helfter et al., 2011). It collects the vertical CO_2 flux (Helfter et al., 2011), turbulent flow quantities (Wood et al., 2010) and other meteorological and greenhouse gas variables. We used the measurements in 2019 to validate our CO_2 model. Specifically, the wind speed and the CO_2 flux were used in the validation. The temporal interval of measurements was half an hour. The CO_2 flux is computed via the procedure described in Section 2.5. We extracted the vertical turbulent flux for CO_2 on a 10 by 10 m^2 grid at 190 m height where the measurement was taken. Note that the temporal averaging window for the turbulent fluctuation in Eq. 7 was selected as 30 min to account for the vortex turnover time. This interval is the same as the averaging cycle in the measurement.

Figure 5 shows the validation results for the CO_2 flux. Overall, good agreement between the simulated CO_2 flux and the measurement at the BT tower has been reached. The trend of the diurnal cycle has been captured by the model and matches well with observations. Specifically, the CO_2 flux remains low in the early morning before sunrise, increases during the morning hours (8 AM to 12 PM), reaches a peak in the afternoon (4 PM to 6 PM), and gradually decreases toward midnight (00.00). As the measurement site is located in a commercial-residential mixed area with limited green spaces, the flux pattern is dominated by anthropogenic emission. Therefore, such a diurnal cycle meets the expectation of human activity patterns within a day. Quantitatively, the magnitudes of fluxes in January, April, and October show very good agreement with observations. Modelled fluxes in July show a consistent pattern as in other seasons, while discrepancy from measurement exists, it is likely due to ill-quality in the observation data.

Figure 6 shows validation of the wind speed. The wind speed on the 10 by 10 m^2 grid at 190 m height corresponding to the measurement location is extracted from the simulation. In the figure, both instantaneous wind speed at a half-hourly interval and its 2-hour moving average daily profile are shown. The general trend of daily variation of wind magnitude (the 2-hour moving average profile) matches that in the measurement. Some residual variances relative to the 2-hour moving average in the model are not aligned with those in the measurement, for example, 6 AM to 9 AM on January 16. These variances are due to turbulent fluctuations in the instantaneous velocity field. The validation results demonstrate that ERA5 provides suitable dynamic boundary conditions for the parent domain and confirm the effectiveness of the nesting strategy in representing processes within the nested domain.

4.2 Validation of biogenic flux

While comparison with the BT tower flux measurement provides the most direct validation of the model, the characteristic in the study area limits the flux validation largely to anthropogenic emission only. Therefore, this subsection focuses on the

https://doi.org/10.5194/egusphere-2026-970
Preprint. Discussion started: 5 March 2026

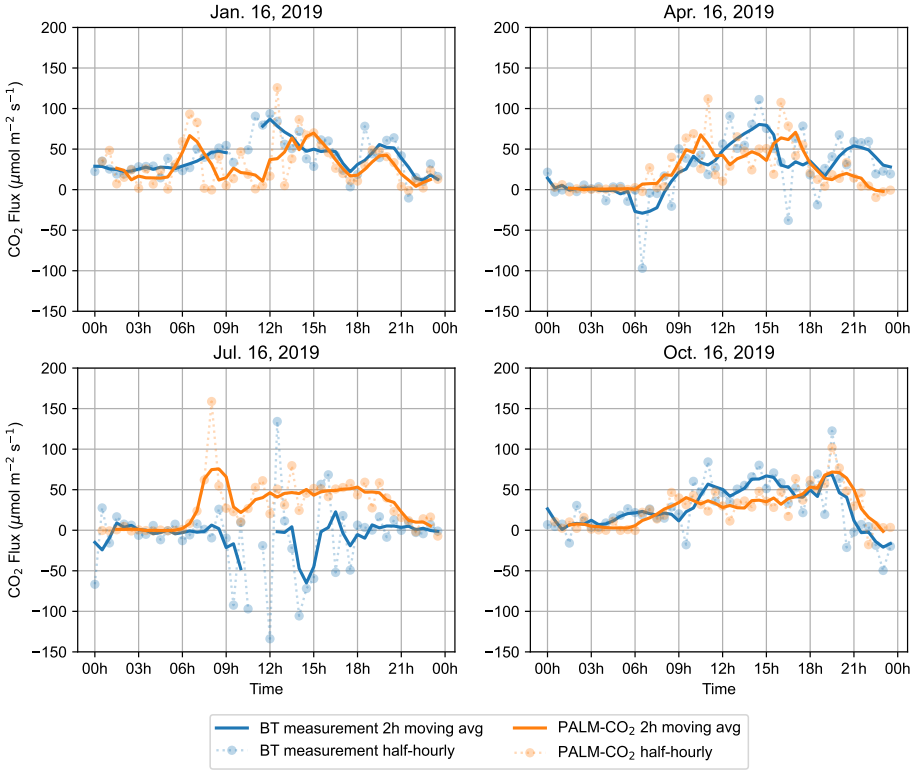

Figure 5. Comparison of modelled **CO_2 fluxes** and BT tower measurements in 2019. Dotted lines and markers show original temporal data at half-hourly resolution for both PALM model and tower measurements. Solid lines show two-hour moving average. All times in the figure are in local time. Break of blue lines show missing data in measurement, e.g. on July 16.

validation of the biogenic flux alone. Due to a lack of in situ measurement, eddy-covariance flux data in another European site with similar vegetation types are used for validation, with the aim of assessing the implementation of the VPRM module.

Part of the green spaces in Regent Park are deciduous forests. For this vegetation type, an EC measurement site at Lanžhot in Czech Republic (CZ-Lnz) is selected for comparison. The data is part of the ICOS (Integrated Carbon Observation System) data product (ICOS RI et al., 2023) which collects data from 39 measurement stations. Situated in a naturally-surrounding town, CZ-Lnz site is mainly influenced by local biogenic fluxes from deciduous forests, i.e. its measurement is the net ecosystem exchange (NEE). We use monthly ensemble average of tower measurement to obtain a daily profile for each month. For modelled NEE, data in one single grid in Regent's Park whose vegetation type is deciduous tree are extracted from the output directly by the VPRM module. Both daily profiles consist of half-hourly data.

https://doi.org/10.5194/egusphere-2026-970
Preprint. Discussion started: 5 March 2026

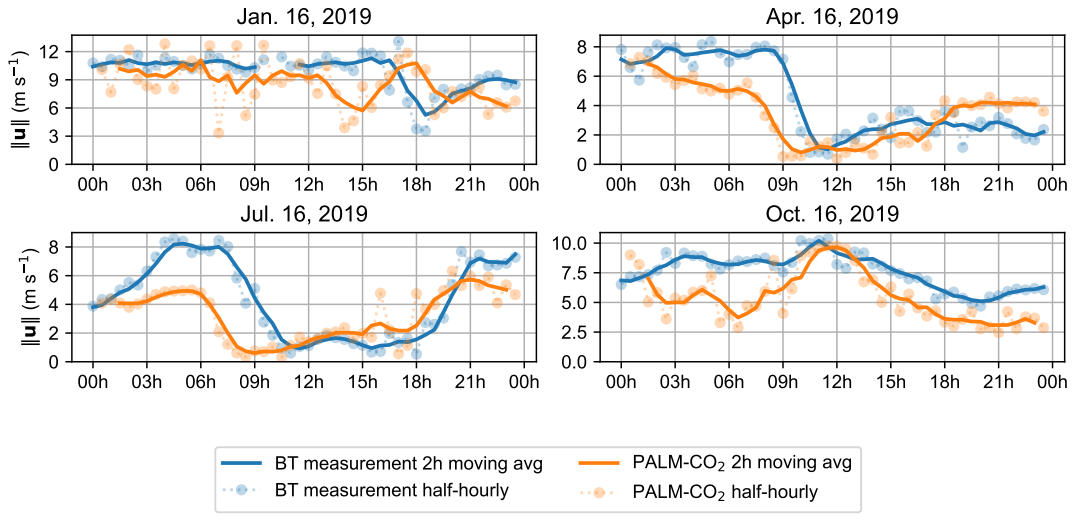

Figure 6. Comparison of modelled **wind speed** and BT tower measurements in 2019. The half-hourly data from PALM model is obtained from the instantaneous wind velocity and thus have a larger variation (dotted line with marker). This variation is eliminated in the 2-hour moving average profile (solid line) and agrees well with measured velocity (blue dotted line or blue solid line).

Figure 7 shows the comparison of modelled NEE with the measured profile. In general, a good agreement has been achieved. Winter times (December, January, February) show smaller NEE, representing a dormant stage of photosynthesis. Summer times (May, June, July) show a larger negative NEE, due to active vegetation take-in. Diurnal cycle is more pronounced in Summer, showing negative NEE during the day and positive NEE at night; while winter time shows a more constant positive NEE throughout the day. Modelled NEE in Camden are significantly larger in March and April (larger sink) and a bit smaller in August, September and October (smaller sink) compared with measurement. These correspond to the budburst and senescence stages of deciduous forests (Duchemin et al., 1999). The offsets in both stages might due to different growing cycles of the forests in the study site and the measurement site. As shown in Figure 8, EVI and LSWI at the probing location used for validation have a sudden increase in March and remain at a mediate level in April. Increasing of both indices contributes to the increase of gross primary production (GPP, Eq. 2). This explains the modelled NEE being larger than the measurement site in CZ-Lnz in budburst stage (in March and April). In the senescence stage (for example, August), on the other hand, EVI reduced to a lower level than in July. This may explain the lower NEE simulated by the model compared to the measurements.

4.3 Urban boundary flow and carbon dioxide concentration

In this subsection, we show results on carbon dioxide concentration and its relation to the height of the Atmospheric Boundary Layer (ABL). Figure 9 shows the CO_2 concentration at the surface level at selected times during a day in January and July. Due to terrain height and building geometries, the surface level at different horizontal places are at different levels. This has been processed and in the figure only the lowest level in the air is plotted. Three snapshots of CO_2 concentration (instantaneous

https://doi.org/10.5194/egusphere-2026-970
Preprint. Discussion started: 5 March 2026

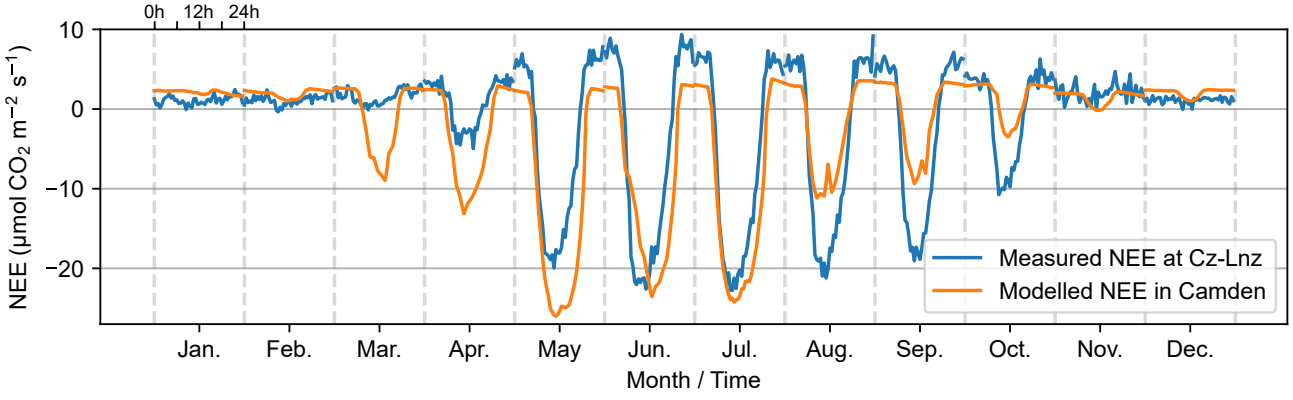

Figure 7. Comparison of monthly 24-hour net ecosystem exchange profile from flux tower measurement and from PALM model. The vegetation type is deciduous trees. The measurement location is at Lanžhot in Czech Republic (CZ-Lnz). Vertical dashed lines denote month boundaries.

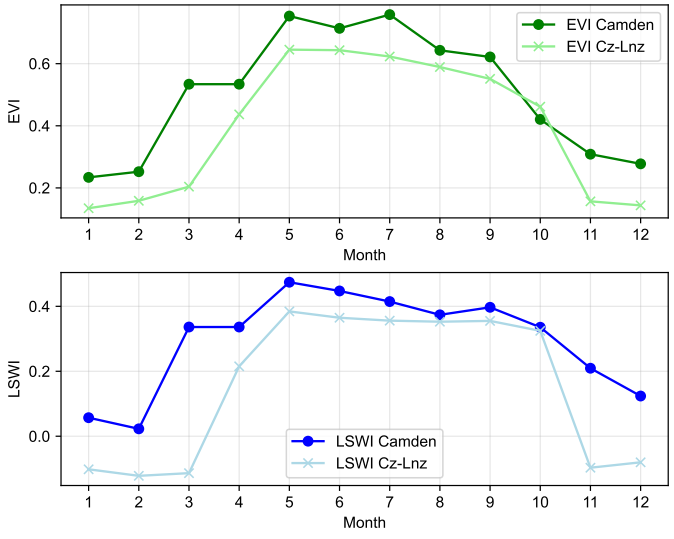

Figure 8. Comparison of monthly EVI and LSWI at two deciduous forests site: Regent Park in Camden, and Lanžhot in Czech Republic (CZ-Lnz). Biogenic fluxes in both sites are compred in Figure 7.

https://doi.org/10.5194/egusphere-2026-970
Preprint. Discussion started: 5 March 2026

field) are shown in the morning 8:30 am, noon 12:30 am, and evening 8:30 pm. In all three snapshots in both January and July, individual large anthropogenic emission locations such as major roads and buildings in the commercial region (lower right in each sub-figures) can be identified. They contribute substantially to the variation of local concentrations. In January, due to a relatively higher wind speed (about 10 m/s, see Fig. 6), advection near the ground level is prominent throughout the day. However, its effect weakens around noon (12:30 pm), due to an increase in upward turbulent flow driven by ground heating in the air. At night, reduced heat turbulence causes a build-up of CO_2 in the region. In July, the wind speed is lower (about 4 m/s, see Fig. 6). In the morning, only limited advection occurs due to weak lateral wind and minimal heat turbulence. Therefore, a large concentration region appears in the dense commercial region (lower right in the sub-figure). At noon, due to increased heat turbulence and upward flow, concentration is reduced in the region. At night, mixed effects from suppressed upward turbulence and increased lateral advection (due to increased wind speed) produce a moderate concentration.

Figure 10 shows the concentration on a $x = 4000$ m cross-section over the domain at different times in January and July. It illustrates the effects of ABL on the variation of the diurnal CO_2 concentration. In general, during morning and night, the boundary layer is shallow, trapping CO_2 below approximately 300 - 400 m, while during the day the ABL height is thicker and inside it CO_2 is well mixed. An exception occurs in the morning (8:30 am) in January when advective transport lifts some plumes above the boundary layer, reducing near-surface accumulation.

Figure 10 also shows the impact of spatial patterns of anthropogenic emissions on CO_2 concentrations within the lower atmospheric layer. As shown in the geography tags, urban land-use types are interwoven from south to north ($+Y$ direction in the figure), alternating commercial districts and green spaces: beginning with parkland (Hyde Park), followed by dense commercial areas (Marylebone), then another parkland and commercial areas (Regent's Park and Camden Town), mixed natural land and residential zones (Hampstead Heath and Highgate). Concentration hotspots correspond to densely populated areas with higher human activities. Throughout the day and in both months, the effect of turbulent dispersion (plumes) can be clearly observed in the figure.

It is noted here that the above pattern is revealed through a fine-scale modelling of the urban topography, anthropogenic and biogenic emissions. The complex CO_2 dispersion pattern indicates the necessity for a fine-resolution model. On this basis, the model can help constrain urban emission pattern in an inversion problem. This conclusion echoes the argument in Brunner et al. (2019).

5 Conclusions

We developed PALM-CO_2, a high-resolution urban carbon dioxide transport modelling framework based on an urban large-eddy simulation code, PALM. The model resolves CO_2 transport at metre-scale resolution (down to 10 metres) under realistic meteorological conditions and explicitly represents urban morphology, including terrain, buildings, and vegetation types. A key novelty of PALM-CO_2, is its fully coupled treatment of fine-scale atmospheric dynamics with spatially detailed anthropogenic and biogenic surface carbon fluxes, enabling the simulation of CO_2 transport processes within the urban canopy layer that cannot be captured by coarser-scale models.

https://doi.org/10.5194/egusphere-2026-970
Preprint. Discussion started: 5 March 2026

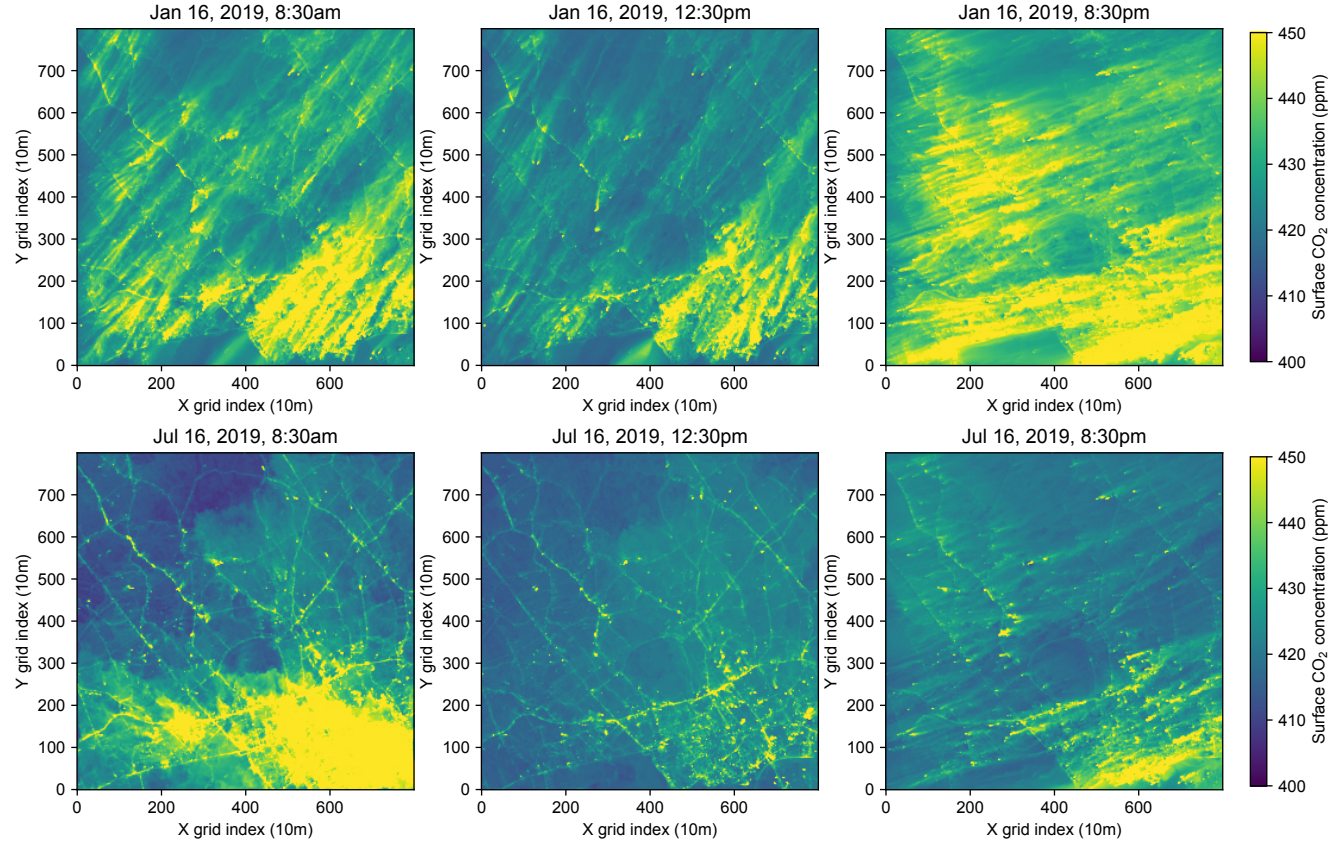

Figure 9. Surface level CO_2 concentration at different times in January (top row) and July (bottom row).

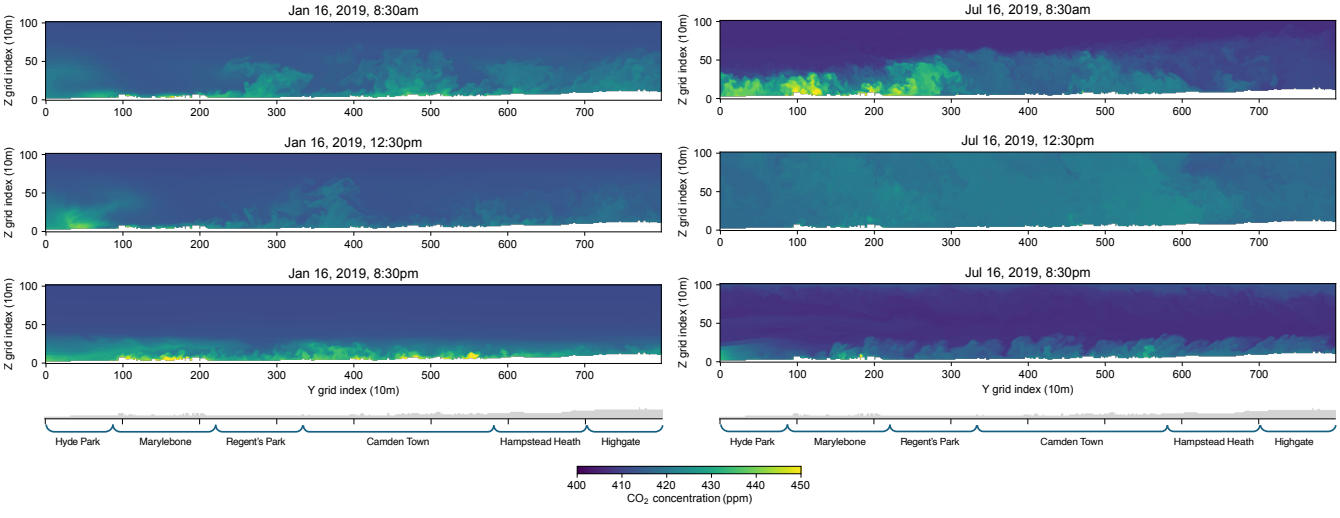

Figure 10. CO_2 concentration at $x = 4000$ m cross-section in the domain at different times in January (left column) and July (right column).

https://doi.org/10.5194/egusphere-2026-970
Preprint. Discussion started: 5 March 2026

The model considers complex urban land surface carbon fluxes from both anthropogenic and biogenic activities. Anthropogenic CO_2 emissions are prescribed at metre-scale resolution (e.g. 10 m) using a bottom-up disaggregation framework that integrates multiple urban data sources, including gas consumption statistics, building energy performance data, industrial point-source inventories, and road transport emissions. Biogenic CO_2 fluxes are represented through the online implementation of the VPRM within PALM. VPRM dynamically computes net ecosystem exchange using PALM-resolved near-surface meteorological conditions and satellite-derived vegetation indices (EVI and LSWI), allowing for a physically consistent coupling between surface carbon exchange and resolved turbulence.

The model is validated against eddy-covariance flux and wind measurements from multiple sites. Within the urban case study domain, simulated turbulent CO_2 fluxes and horizontal wind speeds show good agreement with observations from the BT Tower, where anthropogenic emissions dominate the measured signal. To further assess the biogenic component, PALM-CO_2 is evaluated against flux measurements from the Lanžhot site in the Czech Republic, a deciduous forest ecosystem comparable to the green spaces in the Regent's Park in the study area. Simulated NEE shows captures both dormant and peak growing season behaviour well, while differences in the timing of budburst and senescence reflect climatic contrasts between the two regions, as also indicated by EVI and LSWI. These evaluations demonstrate the robustness of both the transport and surface flux components of PALM-CO_2.

Overall, PALM-CO_2 provides a physically consistent framework for simulating carbon dioxide transport in complex urban environments at metre-scale resolution. By explicitly resolving urban morphology, atmospheric turbulence, and the coupled effects of anthropogenic and biogenic surface fluxes, the model captures multi-scale interactions that cannot be represented in coarser atmospheric transport models. The results demonstrate that fine-scale heterogeneity in emissions, land cover, and boundary-layer dynamics strongly influences urban CO_2 distributions, particularly under stable conditions and during periods of shallow boundary-layer development. These findings underline the importance of high-resolution large-eddy simulation approaches for advancing process-level understanding of urban carbon dynamics and for improving the reliability of urban-scale carbon modelling. PALM-CO_2 thus establishes a robust modelling foundation for future studies investigating urban carbon processes, emission attribution, and the role of cities in the regional carbon cycle.

Code availability. The exact version of the model used to produce the results used in this paper is archived on Zenodo repository under DOI (https://doi.org/10.5281/zenodo.18852193) under GPLv3 License (Li et al., 2026).

Data availability. All input data are either open accessed or proprietary as listed in Table 2. All output data are available upon requests, since file size is too large to be openly hosted.

https://doi.org/10.5194/egusphere-2026-970
Preprint. Discussion started: 5 March 2026

Author contributions. Conceptualization: LL, JZ, FF. Data curation: LL, JZ, FF. Funding acquisition: FF. Investigation: LL, FF. Methodology: LL, FF. Project administration: FF. Software: LL, FF. Validation: LL. Visualization: LL. Writing (original draft preparation): LL. Writing (review and editing): LL, FF.

Competing interests. Authors declare no competing interests.

Acknowledgements. This work is supported by an EPSRC Open Fellowship (EP/X029093/1). This work used the ARCHER2 UK National Supercomputing Service (https://www.archer2.ac.uk). Authors thank Dr Carole Helfter for her help in retrieving BT tower measurement data.

https://doi.org/10.5194/egusphere-2026-970
Preprint. Discussion started: 5 March 2026

References

Ahmadov, R., Gerbig, C., Kretschmer, R., Koerner, S., Neininger, B., Dolman, A., and Sarrat, C.: Mesoscale covariance of transport and CO2 fluxes: Evidence from observations and simulations using the WRF-VPRM coupled atmosphere-biosphere model, Journal of Geophysical Research: Atmospheres, 112, 2007.

Ahmadov, R., Gerbig, C., Kretschmer, R., Körner, S., Rödenbeck, C., Bousquet, P., and Ramonet, M.: Comparing high resolution WRF-VPRM simulations and two global CO2 transport models with coastal tower measurements of CO2, Biogeosciences, 6, 807–817, 2009.

An, X.-q., Zhu, T., Wang, Z.-f., Li, C.-y., and Wang, Y.-s.: A modeling analysis of a heavy air pollution episode occurred in Beijing, Atmospheric Chemistry and Physics, 7, 3103–3114, 2007.

Anav, A., Friedlingstein, P., Kidston, M., Bopp, L., Ciais, P., Cox, P., Jones, C., Jung, M., Myneni, R., and Zhu, Z.: Evaluating the land and ocean components of the global carbon cycle in the CMIP5 earth system models, Journal of Climate, 26, 6801–6843, 2013.

Anders, J. and Maronga, B.: Urban microscale simulations based on a Local Climate Zone wizard: Concept and validation using the PALM model system, Urban Climate, 63, 102 576, 2025.

Brunner, D., Kuhlmann, G., Marshall, J., Clément, V., Fuhrer, O., Broquet, G., Löscher, A., and Meijer, Y.: Accounting for the vertical distribution of emissions in atmospheric CO 2 simulations, Atmospheric Chemistry and Physics, 19, 4541–4559, 2019.

Cai, M., Ren, C., Shi, Y., Chen, G., Xie, J., and Ng, E.: Modeling spatiotemporal carbon emissions for two mega-urban regions in China using urban form and panel data analysis, Science of the Total Environment, 857, 159 612, 2023.

Christen, A., Coops, N., Crawford, B., Kellett, R., Liss, K., Olchovski, I., Tooke, T., Van Der Laan, M., and Voogt, J.: Validation of modeled carbon-dioxide emissions from an urban neighborhood with direct eddy-covariance measurements, Atmospheric Environment, 45, 6057–6069, 2011.

Copernicus Atmosphere Monitoring Service: CAMS global greenhouse gas reanalysis (EGG4), Copernicus Atmosphere Monitoring Service (CAMS) Atmosphere Data Store, https://doi.org/10.24381/cda4ed31, assessed on 2025-11-11, 2021.

Crippa, M., Solazzo, E., Huang, G., Guizzardi, D., Koffi, E., Muntean, M., Schieberle, C., Friedrich, R., and Janssens-Maenhout, G.: High resolution temporal profiles in the Emissions Database for Global Atmospheric Research, Scientific data, 7, 121, 2020.

Department for Energy Security and Net Zero: Lower and Middle Super Output Areas Gas Consumption, https://www.gov.uk/government/statistics/lower-and-middle-super-output-areas-gas-consumption, published 31 March 2015, 2015.

Department for Levelling Up, Housing & Communities: Energy Performance of Buildings Data: England and Wales, https://epc.opendatacommunities.org/, 2025.

Dhakal, S.: GHG emissions from urbanization and opportunities for urban carbon mitigation, Current Opinion in Environmental Sustainability, 2, 277–283, 2010.

Duchemin, B., Goubier, J., and Courrier, G.: Monitoring phenological key stages and cycle duration of temperate deciduous forest ecosystems with NOAA/AVHRR data, Remote Sensing of Environment, 67, 68–82, 1999.

Environment Agency: National LIDAR Programme, Dataset, Environment Agency / data.gov.uk, https://www.data.gov.uk/dataset/f0db0249-f17b-4036-9e65-309148c97ce4/national-lidar-programme, elevation data at 1 m resolution for England; © Environment Agency database rights., 2025.

European Space Agency (ESA): Harmonized Sentinel-2 MSI: MultiSpectral Instrument, Level-2A (SR), assessed from Google Earth Engine on 2025-11-11, 2025.

https://doi.org/10.5194/egusphere-2026-970
Preprint. Discussion started: 5 March 2026

Friedlingstein, P., O'Sullivan, M., Jones, M. W., Andrew, R. M., Bakker, D. C. E., Hauck, J., Landschützer, P., Le Quéré, C., Luijkx, I. T., Peters, G. P., Peters, W., Pongratz, J., Schwingshackl, C., Sitch, S., Canadell, J. G., Ciais, P., Jackson, R. B., Alin, S. R., Anthoni, P., Barbero, L., Bates, N. R., Becker, M., Bellouin, N., Decharme, B., Bopp, L., Brasika, I. B. M., Cadule, P., Chamberlain, M. A., Chandra, N., Chau, T.-T.-T., Chevallier, F., Chini, L. P., Cronin, M., Dou, X., Enyo, K., Evans, W., Falk, S., Feely, R. A., Feng, L., Ford, D. J., Gasser, T., Ghattas, J., Gkritzalis, T., Grassi, G., Gregor, L., Gruber, N., Gürses, O., Harris, I., Hefner, M., Heinke, J., Houghton, R. A., Hurtt, G. C., Iida, Y., Ilyina, T., Jacobson, A. R., Jain, A., Jarníková, T., Jersild, A., Jiang, F., Jin, Z., Joos, F., Kato, E., Keeling, R. F., Kennedy, D., Klein Goldewijk, K., Knauer, J., Korsbakken, J. I., Körtzinger, A., Lan, X., Lefèvre, N., Li, H., Liu, J., Liu, Z., Ma, L., Marland, G., Mayot, N., McGuire, P. C., McKinley, G. A., Meyer, G., Morgan, E. J., Munro, D. R., Nakaoka, S.-I., Niwa, Y., O'Brien, K. M., Olsen, A., Omar, A. M., Ono, T., Paulsen, M., Pierrot, D., Pocock, K., Poulter, B., Powis, C. M., Rehder, G., Resplandy, L., Robertson, E., Rödenbeck, C., Rosan, T. M., Schwinger, J., Séférian, R., Smallman, T. L., Smith, S. M., Sospedra-Alfonso, R., Sun, Q., Sutton, A. J., Sweeney, C., Takao, S., Tans, P. P., Tian, H., Tilbrook, B., Tsujino, H., Tubiello, F., van der Werf, G. R., van Ooijen, E., Wanninkhof, R., Watanabe, M., Wimart-Rousseau, C., Yang, D., Yang, X., Yuan, W., Yue, X., Zaehle, S., Zeng, J., and Zheng, B.: Global Carbon Budget 2023, Earth System Science Data, 15, 5301–5369, https://doi.org/10.5194/essd-15-5301-2023, 2023.

Gerbig, C. and Koch, F.-T.: Biosphere-atmosphere exchange fluxes for CO2 from the Vegetation Photosynthesis and Respiration Model VPRM for 2022-2023, https://doi.org/10.18160/R5HS-YKW0, 2024.

Guevara, M., Jorba, O., Tena, C., Denier van der Gon, H., Kuenen, J., Elguindi, N., Darras, S., Granier, C., and Pérez García-Pando, C.: Copernicus Atmosphere Monitoring Service TEMPOral profiles (CAMS-TEMPO): global and European emission temporal profile maps for atmospheric chemistry modelling, Earth System Science Data, 13, 367–404, 2021.

Helfter, C., Famulari, D., Phillips, G. J., Barlow, J. F., Wood, C. R., Grimmond, C. S. B., and Nemitz, E.: Controls of carbon dioxide concentrations and fluxes above central London, Atmospheric Chemistry and Physics, 11, 1913–1928, 2011.

Helfter, C., Tremper, A. H., Halios, C. H., Kotthaus, S., Bjorkegren, A., Grimmond, C. S. B., Barlow, J. F., and Nemitz, E.: Spatial and temporal variability of urban fluxes of methane, carbon monoxide and carbon dioxide above London, UK, Atmospheric Chemistry and Physics, 16, 10 543–10 557, 2016.

Hersbach, H., Bell, B., Berrisford, P., Hirahara, S., Horányi, A., Muñoz-Sabater, J., Nicolas, J., Peubey, C., Radu, R., Schepers, D., et al.: The ERA5 global reanalysis, Quarterly journal of the royal meteorological society, 146, 1999–2049, 2020.

Heus, T., van Heerwaarden, C. C., Jonker, H. J., Pier Siebesma, A., Axelsen, S., Van Den Dries, K., Geoffroy, O., Moene, A., Pino, D., De Roode, S., et al.: Formulation of the Dutch Atmospheric Large-Eddy Simulation (DALES) and overview of its applications, Geoscientific Model Development, 3, 415–444, 2010.

ICOS RI, Aalto, J., Aiguier, T., Alivernini, A., Aluome, C., Andersson, T., Arriga, N., Aurela, M., Back, J., Barten, S., Baur, T., Bazot, S., Beauclair, P., Becker, N., Becker, N., Belelli Marchesini, L., Bergström, G., Bernhofer, C., Berveiller, D., Biermann, T., Bloor, J., Bodson, B., Bogaerts, G., Bortoli, M., Bosio, I., Brut, A., Brümmer, C., Buchmann, N., Buysse, P., Båth, A., Calandrelli, D., Cavagna, M., Ceschia, E., Chabbi, A., Chebbi, W., Chianucci, F., Chipeaux, C., Chopin, H., Claverie, N., Cobbe, I., Colosse, D., Conte, A., Corsanici, R., Courtois, P., Coyle, M., Crill, P., Cuntz, M., Cuocolo, D., Czerný, R., DEPUYDT, J., Darenová, E., Darsonville, O., De Ligne, A., De Meulder, T., De Simon, G., Decau, M.-L., Dell'Acqua, A., Delorme, J.-P., Delpierre, N., Demoulin, L., Denou, J.-L., Di Matteo, B., Di Tommasi, P., Dienstbach, L., Dignam, R., Dolfus, D., Domec, J.-C., Douxfils, B., Dufrêne, E., Dumont, B., Durand, B., Eichelmann, U., Engelmann, T., Esposito, A., Esser, O., Etzold, S., Eugster, W., Famulari, D., Fares, S., Faurès, A., Feigenwinter, I., Feldmann, I., Fincham, W., Fischer, M., Foltýnová, L., Friborg, T., Galliot, J.-N., Garcia Quiros, I., Garrigou, C., Gasbarra, D., Gessler, A., Gharun, M., Gianelle, D., Gimper, S., Goded, I., Graf, A., Granouillac, F., Grenier, M., Grudd, H., Grünwald, T., Guillot, T., Harvey, D., Hatakka,

https://doi.org/10.5194/egusphere-2026-970
Preprint. Discussion started: 5 March 2026

J., Haustein, A., Hehn, M., Heinesch, B., Helfter, C., Heliasz, M., Holst, J., Holst, T., Hug, C., Häni, M., Hörtnagl, L., Ibrom, A., Ilardi, F., Jackowicz-Korczynski, M. A., Janssens, I., Jensen, R., Jocher, G., Joetzjer, E., Jones, M., Kempf, J., Kettler, M., Kljun, N., Klumpp, K., Kolari, P., Korrensalo, A., Kowalska, N., Kozii, N., Krejza, J., Kristoffersson, A., Kruijt, B., Kruszewski, A., Kumar, S., Kummer, S., Laakso, H., Lafont, S., Lange Rønn, E., Larmanou, E., Laurila, T., Leeson, S., Lefevre, L., Lehner, I., Lemaire, B., Levula, J., Levy, P., Liechti, K., Lily, J.-B., Limousin, J.-M., Linderson, M.-L., Lindgren, K., Lohila, A., Longdoz, B., Lootens, R., Loubet, B., Loustau, D., Lundin, E., López-Blanco, E., Löfvenius, P., Magliulo, V., Mammarella, I., Manco, A., Manise, T., Marcolla, B., Marek, M. V., Marklund, P., Marloie, O., Martin, R., Martin Saint Paul, N., Marty, M., Matilainen, T., Mattes, J., Matteucci, M., Mauder, M., Meier, P., Meire, A., Meis, J., Mensah, C., Michaud, L., Minerbi, S., Moderow, U., Montagnani, L., Moretti, V., Morfin, A., Mullinger, N., Mäkelä, T., Männikkö, M., Männistö, E., Mölder, M., Møller, F., Naiken, A., Naseer, M., Nemitz, E., Nezval, O., Nilsson, M., Orgun, A., Ottosson-Löfvenius, M., Ourcival, J.-M., Paasch, S., Pavelka, M., Peichl, M., Perot-Guillaume, C., Perrot, C., Pihlatie, M., Pilegaard, K., Piret, A., Prasse, H., Pumpanen, J., Rainne, J., Rakos, N., Rasmussen, L., Rebmann, C., Rinne, J., Rodeghiero, M., Roland, M., Rudd, D., Røjle Christensen, T., Schaarup Sørensen, J., Schmidt, M., Schmidt, P., Schmitt Oehler, M., Schrader, F., Segers, J., Simioni, G., Smith, P., Snellen, H., Sorgi, T., Soudani, K., Staník, K., Staudinger, M., Stecher, M., Stutz, T., Suopajärvi, S., Sutter, F., Taipale, R., Tallec, T., Tenca, F., Thimonier Rickenmann, A., Thyrion, T., Tomelleri, E., Tosca, M., Trotsiuk, V., Trusina, J., Tuittila, E.-S., Tuovinen, J.-P., Tyssandier, J., Tülp, H., Van Look, J., Varjonen, S., Vesala, T., Vescovo, L., Vincent, G., Vincke, C., Vitale, L., Vágner, L., Waldner, P., Wiesen, R., Winck, B., Yeung, K., Zampedri, R., Zawilski, B., Zenone, T., Zimmermann, S., Zweifel, R., van Dijk, N., van der Molen, M., Öquist, M., Šigut, L., Šlížek, J., and ICOS ETC: Ecosystem final quality (L2) product in ETC-Archive format - INTERIM release 2023-2, https://doi.org/10.18160/JYAR-7YEH, 2023.

Järvi, L., Havu, M., Ward, H. C., Bellucco, V., McFadden, J. P., Toivonen, T., Heikinheimo, V., Kolari, P., Riikonen, A., and Grimmond, C. S. B.: Spatial modeling of local-scale biogenic and anthropogenic carbon dioxide emissions in Helsinki, Journal of Geophysical Research: Atmospheres, 124, 8363–8384, 2019.

Jiang, S., Wang, J., Li, C., Ou, J., Duan, P., and Li, L.: Identification of no-fly zones for delivery drone path planning in various urban wind environments, Physics of Fluids, 36, 2024.

Khan, B., Banzhaf, S., Chan, E. C., Forkel, R., Kanani-Sühring, F., Ketelsen, K., Kurppa, M., Maronga, B., Mauder, M., Raasch, S., et al.: Development of an atmospheric chemistry model coupled to the PALM model system 6.0: Implementation and first applications, Geoscientific Model Development, 14, 1171–1193, 2021.

Li, L., Zheng, J., and Fang, F.: PALM-CO2 (v01), https://doi.org/10.5281/zenodo.18852193, 2026.

Lian, J., Bréon, F.-M., Broquet, G., Lauvaux, T., Zheng, B., Ramonet, M., Xueref-Remy, I., Kotthaus, S., Haeffelin, M., and Ciais, P.: Sensitivity to the sources of uncertainties in the modeling of atmospheric CO2 concentration within and in the vicinity of Paris, Atmospheric Chemistry and Physics, 21, 10 707–10 726, 2021.

Lin, D., Zhang, J., Khan, B., Katurji, M., and Revell, L. E.: GEO4PALM v1.1: an open-source geospatial data processing toolkit for the PALM model system, Geoscientific Model Development, 17, 815–845, https://doi.org/10.5194/gmd-17-815-2024, 2024.

London Datastore: London Atmospheric Emissions Inventory (LAEI) 2019, https://data.london.gov.uk/dataset/london-atmospheric-emissions-inventory-laei-2019-e758q/, 2023.

Mahadevan, P., Wofsy, S. C., Matross, D. M., Xiao, X., Dunn, A. L., Lin, J. C., Gerbig, C., Munger, J. W., Chow, V. Y., and Gottlieb, E. W.: A satellite-based biosphere parameterization for net ecosystem CO2 exchange: Vegetation Photosynthesis and Respiration Model (VPRM), Global Biogeochemical Cycles, 22, https://doi.org/https://doi.org/10.1029/2006GB002735, 2008.

https://doi.org/10.5194/egusphere-2026-970
Preprint. Discussion started: 5 March 2026

Marcotullio, P. J., Sarzynski, A., Albrecht, J., Schulz, N., and Garcia, J.: The geography of global urban greenhouse gas emissions: An exploratory analysis, Climatic Change, 121, 621–634, 2013.

Maronga, B., Banzhaf, S., Burmeister, C., Esch, T., Forkel, R., Fröhlich, D., Fuka, V., Gehrke, K. F., Geletič, J., Giersch, S., et al.: Overview of the PALM model system 6.0, Geoscientific Model Development, 13, 1335–1372, 2020.

Neves, T., Fisch, G., and Raasch, S.: Local convection and turbulence in the Amazonia using large eddy simulation model, Atmosphere, 9, 399, 2018.

OpenStreetMap contributors: Planet dump retrieved from https://planet.osm.org , https://www.openstreetmap.org, 2017.

Ordnance Survey (GB): OS MasterMap Building Height Attribute [CSV Geospatial Data], Accessed via EDINA Digimap Ordnance Survey Service, https://digimap.edina.ac.uk, scale 1:2500; Tiles: tq27nw, tq28sw, tq28nw, tq27ne, tq28se, tq28ne, tq37nw, tq38sw, tq38nw; Updated: 30 August 2019; Downloaded: 2025-07-02 12:14:06.331, 2019a.

Ordnance Survey (GB): OS MasterMap Topography Layer [GeoPackage Geospatial Data], Accessed via EDINA Digimap Ordnance Survey Service, https://digimap.edina.ac.uk, scale 1:1250; Tiles: GB; Updated: 28 November 2019; Downloaded: 2025-07-02 12:14:42.54, 2019b.

Ordnance Survey (GB): OS Terrain 50 [ASC Geospatial Data], Accessed via EDINA Digimap Ordnance Survey Service, https://digimap.edina.ac.uk, scale 1:50000; Tiles: sp90, su94, su95, su96, su97, su98, su99, tl00, tl10, tl20, tl30, tl40, tl50, tl60, tq04, tq05, tq06, tq07, tq08, tq09, tq14, tq15, tq16, tq17, tq18, tq19, tq24, tq25, tq26, tq27, tq28, tq29, tq34, tq35, tq36, tq37, tq38, tq39, tq44, tq45, tq46, tq47, tq48, tq49, tq54, tq55, tq56, tq57, tq58, tq59, tq64, tq65, tq66, tq67, tq68, tq69; Updated: 29 May 2019; Downloaded: 2025-07-02, 2019c.

Pfafferott, J., Rißmann, S., Sühring, M., Kanani-Sühring, F., and Maronga, B.: Building indoor model in PALM model system 6.0: Indoor climate, energy demand, and the interaction between buildings and the urban climate, Geoscientific Model Development Discussions, 2020, 1–11, 2020.

Pillai, D., Gerbig, C., Marshall, J., Ahmadov, R., Kretschmer, R., Koch, T., and Karstens, U.: High resolution modeling of CO2 over Europe: implications for representation errors of satellite retrievals, Atmospheric Chemistry and Physics, 10, 83–94, 2010.

Pillai, D., Gerbig, C., Ahmadov, R., Rödenbeck, C., Kretschmer, R., Koch, T., Thompson, R., Neininger, B., and Lavrié, J.: High-resolution simulations of atmospheric CO2 over complex terrain–representing the Ochsenkopf mountain tall tower, Atmospheric Chemistry and Physics, 11, 7445–7464, 2011.

Skamarock, W. C., Klemp, J. B., Dudhia, J., Gill, D. O., Liu, Z., Berner, J., Wang, W., Powers, J. G., Duda, M. G., Barker, D. M., et al.: A description of the advanced research WRF version 4, NCAR tech. note ncar/tn-556+ str, 145, 2019.

Smith, A. C., Li, L., Xiang, J., and Fang, F.: Machine learning-based land-use regression models for predicting carbon dioxide concentrations in San Francisco Bay area, Environmental Earth Sciences, 84, 539, 2025.

Stagakis, S., Brunner, D., Li, J., Backman, L., Karvonen, A., Constantin, L., Järvi, L., Havu, M., Chen, J., Emberger, S., et al.: Intercomparison of biogenic CO2 flux models in four urban parks in the city of Zurich, Biogeosciences, 22, 2133–2161, 2025.

Wilby, R. L. and Perry, G. L.: Climate change, biodiversity and the urban environment: a critical review based on London, UK, Progress in physical geography, 30, 73–98, 2006.

Wood, C., Lacser, A., Barlow, J. F., Padhra, A., Belcher, S. E., Nemitz, E., Helfter, C., Famulari, D., and Grimmond, C.: Turbulent flow at 190 m height above London during 2006–2008: a climatology and the applicability of similarity theory, Boundary-Layer Meteorology, 137, 77–96, 2010.

Zanaga, D., Van De Kerchove, R., Daems, D., De Keersmaecker, W., Brockmann, C., Kirches, G., Wevers, J., Cartus, O., Santoro, M., Fritz, S., Lesiv, M., Herold, M., Tsendbazar, N.-E., Xu, P., Ramoino, F., and Arino, O.: ESA WorldCover 10 m 2021 v200, https://doi.org/10.5281/zenodo.7254221, 2022.